Unveiling Strong Ion–Electron–Lattice Coupling and Electronic Antidoping in Hydrogenated Perovskite Nickelate

Lei Gao, Huimin Wang, Fanqi Meng, Huining Peng, Xiangyu Lyu, Mingtong Zhu, Yuqian Wang, Chao Lu, Jin Liu, Ting Lin, Ailing Ji, Qinghua Zhang,* Lin Gu, Pu Yu, Sheng Meng,* Zexian Cao, and Nianpeng Lu*

Despite being highly promising for applications in emergent electronic devices, decoding both the ion–electron–lattice coupling in correlated materials at the atomic scale and the electronic band structure remains a big challenge due to the strong and complex correlation among these degrees of freedom. Here, taking an epitaxial thin film of perovskite nickelate $NdNiO_3$ as a model system, hydrogen-ion-induced giant lattice distortion and enhanced NiO_6 octahedra tilting/rotation are demonstrated, which leads to a new robust hydrogenated $HNdNiO_3$ phase with lattice expansion larger than 10% on a series of substrates. Moreover, under the effect of ion–electron synergistic doping, it is found that the proposed electronic antidoping, i.e., the doped electrons mainly fill the ground-state oxygen 2p holes instead of changing the Ni oxidation state from Ni^{3+} to Ni^{2+}, dominates the metal–insulator transition. Meanwhile, lattice modification with enhanced Ni–O–Ni bond tilting or rotation mainly modifies the orbital density of states near the Fermi level. Last, by electric-field-controlled hydrogen-ion intercalation and its strong coupling to the lattice and electron charge, selective micrometer-scale patterns with distinct structural and electronic states are fabricated. The results provide direct evidence for a strong ion–electron–lattice coupling in correlated physics and exhibit its potential applications in designing novel materials and devices.

1. Introduction

Due to strong coupling among the degrees of freedom (ion, electron, and lattice), when ions are intercalated into the crystal lattice, the crystal symmetry and corresponding crystal field splitting can be dramatically altered by changing chemical bonds or polyhedral rotation patterns.[1–4] Meanwhile, the accompanying charge doping could change the electronic band structure and/or orbital occupations. These effects subsequently generate a series of novel electronic states and exotic physical phenomena and functionalities.[5–7] Among these properties, metal–insulator transition forms a central topic in condensed matter physics with tremendous applications.[8,9] Compared with the conventional modulation methods, such as strain, high pressure, chemical doping, and electrostatic effect, ionic intercalation especially by the recently developed ionic liquid gating (H^+, O^{2-}, Li^+, or other types of ions), has been proved an effective way to induce the metal–insulator transition and attracted wide-range

L. Gao, H. Wang, X. Lyu, M. Zhu, Y. Wang, C. Lu, J. Liu, T. Lin, A. Ji,
Q. Zhang, S. Meng, Z. Cao, N. Lu
Beijing National Laboratory for Condensed Matter Physics and Institute
of Physics
Chinese Academy of Science
Beijing 100190, China
E-mail: zqh@iphy.ac.cn; smeng@iphy.ac.cn; lunianpeng@iphy.ac.cn
H. Wang, M. Zhu, J. Liu, T. Lin, A. Ji, Q. Zhang, S. Meng, Z. Cao, N. Lu
School of Physical Sciences
University of Chinese Academy of Sciences
Beijing 100190, China
F. Meng, L. Gu
School of Materials Science and Engineering
Tsinghua University
Beijing 100084, China

H. Peng, P. Yu
State Key Laboratory of Low Dimensional Quantum Physics and
Department of Physics
Tsinghua University
Beijing 100084, China
X. Lyu
College of Materials Science and Opto-Electronic Technology
University of Chinese Academy of Sciences
Beijing 101408, China
P. Yu
Frontier Science Center for Quantum Information
Beijing 100084, China
S. Meng, Z. Cao, N. Lu
Songshan Lake Materials Laboratory
Dongguan, Guangdong 523808, China

interests both in fundamental research and practical applications.[2–5,10] Then, based on these facts we know that coupling among the three degrees of freedom of ion–electron–lattice plays a significant role in determining the final physical properties of correlated materials, and through clarifying the correlation among them, it can greatly prompt and deepen our understanding on the underlying physics and the metal–insulator transition mechanism.

Nickelates with the general formula $RNiO_3$ (R = rare earth) are typical correlated perovskites for fascinating physical properties, especially for the tunable and modulated metal–insulator transition.[11–14] Specifically, in recent years hydrogen-ion intercalation has become an effective pathway to induce the metal–insulator transition for nickelates. Based on these, many findings focusing on the emergent electronic devices were exploited, such as in the research fields of energy conversion, biosensing and neuromorphic devices.[15–18] Despite many interesting functional properties have been demonstrated in hydrogenated perovskite nickelates, the direct atomic-scale observation of lattice modification with oxygen octahedral rotations and tiltings and the corresponding structural transformation during the ion intercalation, has not been investigated yet. Moreover, the underlying modulation mechanisms in the electronic structure and orbital filling during hydrogen-ion intercalation are also waiting to be clarified. Then, we know that it provides an ideal platform and correlated material to investigate the ion–electron–lattice coupling and interesting physical properties in the perovskite nickelate.

In this work, with epitaxial neodymium nickelate ($NdNiO_3$, NNO) thin film as a model system, electric-field-controlled hydrogen-induced structural phase transformation and metal–insulator transition in the crystallographic and electronic band structure were carefully investigated. Through ionic liquid gating, we first realized the reversible phase transformation between NNO and a newly formed hydrogenated NNO phase, along with a giant lattice expansion of larger than 10% on a series of substrates. The new hydrogenated NNO phase exhibits highly structural order and good stability. Due to hydrogen ions binding, the atomic scale lattice shows clear modification and remarkably enhanced oxygen octahedral tiltings or rotations. Moreover, the measured X-ray absorption spectra combining with the first-principle calculations, reveal that contrary to the previously proposed redox reaction between Ni^{3+} and Ni^{2+}, the electrons donated from intercalated hydrogen mainly fill the ground-state oxygen 2p holes in the negative charge-transfer band structure of NNO. Through comparing with the hydrogen-ion-induced structural lattice distortion, it is found that this proposed electronic antidoping mechanism dominates the metal–insulator transition. Finally, by virtue of the strong ion–electron–lattice coupling, selective micropatterns with distinct surface profiles and electrical properties were demonstrated.

2. Results

2.1. Hydrogen Ion Intercalation Induced Reversible Phase Transformation with Giant Lattice Modification

In our experiment, ionic liquid gating was performed on high quality epitaxial NNO thin film grown on $LaAlO_3$(001) (LAO) substrate by pulsed laser deposition, in which hydrogen ion can be intercalated into the lattice. Due to the strong coupling among the degrees of freedom of ion, charge and lattice, structural lattice distortion and empty orbital filling can be realized under the synergistic ion–electron doping (**Figure 1**a). The two-terminal system was utilized to achieve gating by using the ionic liquid electrolyte (Figure 1b). When a positive gate voltage (V_G) is applied across such electrolytes, mobile cations (anions) drift and accumulate at the electrolyte–film (electrode) interface. Due to the created strong positive electric field at the interface, the H^+ ions could be inserted into the crystal lattice, and the compensated charges would be synergistically doped (for electric neutrality) based on electrochemical mechanism.[4,19,20]

Bulk NNO adopts an $GdFeO_3$-type orthorhombic structure[11,13] with space group Pbnm (a = 5.3891 Å, b = 5.3816 Å, c = 7.6101 Å), which also could be indexed in a pseudocubic unit cell with a_{pc} = 3.805 Å. When coherently grown on LAO substrate (a_{pc} = 3.792 Å), it experiences a compressive strain of −0.3%. To show the ionic liquid gating induced phase transformation, we performed ex situ X-ray diffraction (XRD) on the high-quality NNO film. As shown in Figure 1c, with +4 V gating voltage, the XRD peak position for the (002) diffraction plane shows a significant change from 47.64° to 41.80°, corresponding to a giant lattice expansion ≈13.2% along the c-axis (out-of-plane direction). As confirmed by the out-of-plane θ–2θ scan and reciprocal space mapping (RSM) measurement of NNO and the newly formed phase (Figure 1c and Figure S1, Supporting Information), the thin film is still fully strained to the substrate with the same in-plane lattice constant despite such large expansion. Due to the strong substrate restriction, the NNO film, not like bulk materials that are prone to crushing due to ion intercalation,[21] maintains the lattice integrity very well which also help us investigate its intrinsic physical properties.

To explore the ionic liquid gating process and reversibility of the phase transformation, we further performed the in situ XRD measurement (Figure 1d and Figure S2, Supporting Information). During the gating, we noticed that with applying +4 V voltage, diffraction peak of the new phase appeared rapidly in a few minutes, meanwhile the NNO diffraction peak gradually became weak and disappeared finally. While by applying a reverse gating voltage of −4 V, the newly formed phase returned completely to the initial state. The phase-transformation process, in which the diffraction line decreased in its intensity with a concurrent increase in the intensity of a new diffraction line at lower diffraction angle, strongly suggests that it is a two-phase reaction (like the $LiFePO_4$/$FePO_4$ transition in lithium ion battery) rather than a single-phase continuous miscibility reaction with the diffraction line shifting continuously.[22,23]

To determine the phase transformation mechanism, we carried out secondary-ion mass spectroscopy (SIMS) measurements on NNO and the new phase to analyze the depth profiling of chemical composition (Figure 1e). We found that there exists a large amount of hydrogen in the new phase. The H concentration is about two order of magnitude larger than that in pristine NNO phase and keeps nearly constant from the top surface to the film/substrate interface, which indicates that hydrogen ions uniformly distribute in the gated thin film. Furthermore, through deuterium (D) and ^{18}O isotope calibration by the developed heavy water (D_2O) doped ionic liquid and $^{18}O_2$ gas, we found that the deuterium ion uniformly distributes inside the H(D)-NNO, while

ADVANCED
SCIENCE NEWS
www.advancedsciencenews.com

**ADVANCED
MATERIALS**
www.advmat.de
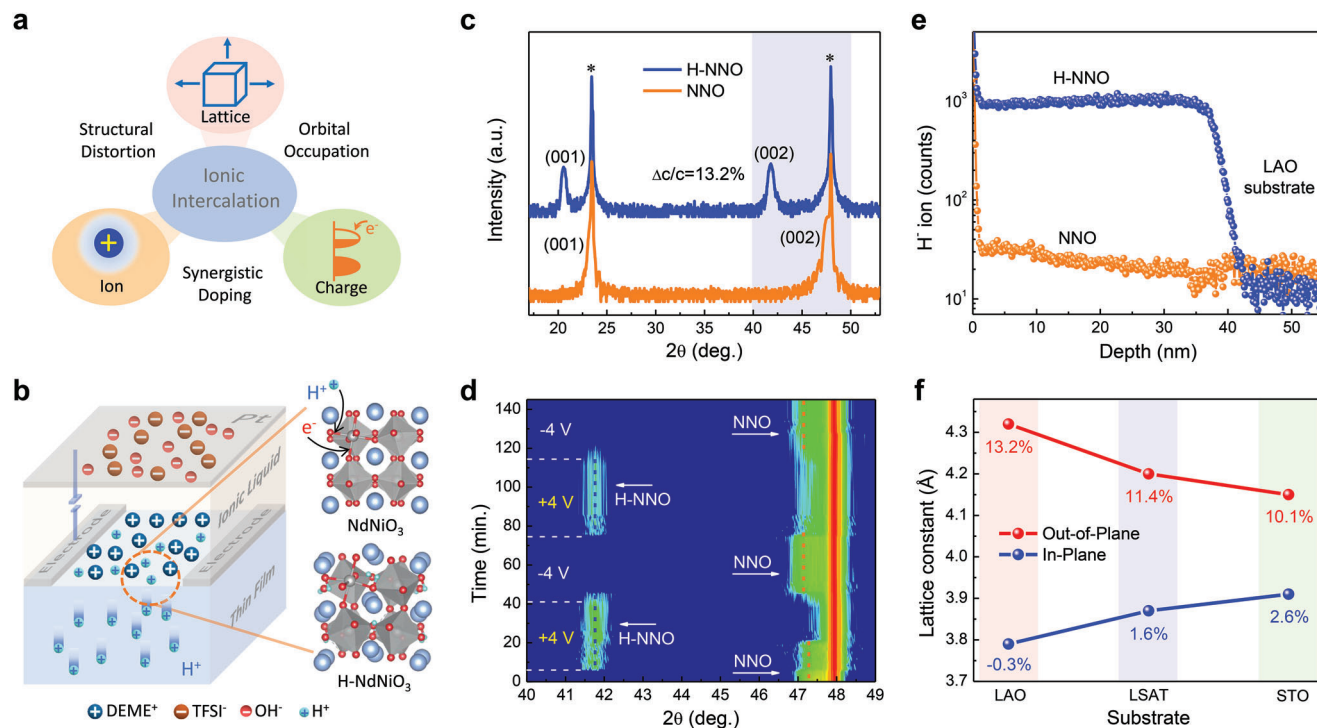
Figure 1. Electric-field-controlled hydrogen ion intercalation induced new phase H-NNO with giant lattice modification and reversible phase transformation. a) Coupling among multiple degrees of freedom of ion, charge and lattice, in which the charge assisted ionic intercalation through synergistic doping effect can induce the lattice expansion and the charge doping. b) Schematic diagram of ionic liquid gating, in which the electric double layer provides the driving force for hydrogen intercalation and the trace amount of H_2O offers the source of hydrogen ions. c) Hydrogen-intercalation-induced phase transformation between NNO and the new phase H-NNO with giant lattice expansion of maximum 13.2% on LAO substrate. d) In situ XRD of the ionic liquid gating induced giant lattice expansion and reversible phase transformation from NNO to H-NNO. The red and blue dashed lines represent diffraction peaks of NNO and H-NNO films, respectively. e) Depth profiles of H ions for secondary-ion mass spectroscopy measurement of NNO and H-NNO on LAO substrate. f) Strain-dependent hydrogen ion intercalation induced out-of-plane lattice variation for coherent in-plane lattice strain on different substrates.

negligible isotope [18]O could be detected (Note 1 and Figures S3 and S4, Supporting Information). Then, the ionic liquid gating induced structural transformation was confirmed to be the hydrogenation process. Moreover, through the gate voltage (V_G)-dependent in situ XRD measurement, the threshold voltage for the phase transition is determined to be between 1.2 V and 1.3 V (Note 2 and Figure S5, Supporting Information), which is also consistent with the water hydrolysis mechanism in ionic liquid gating.[4]

Except the electrochemical intercalation and chemical reduction methods,[16,24] H-spillover with Pt catalyst also can be used to realize the hydrogenation of perovskite nickelates.[15,17,25] In order to comprehensively study the hydrogenation phenomenon, we also formed hydrogenated NNO using the Pt catalytic method. As shown in Figure S6 (Supporting Information), we obtained the same result of hydrogenated NNO using the two different approaches. Considering the only notable hydrogenated phase with the fixed crystal lattice constant shown in XRD, we conjecture that the new robust phase is a compound with fixed chemical stoichiometric. Based on these findings, we tentatively assigned the new phase as hydrogenated $NdNiO_3$ (H-NNO).

The stability of the newly formed H-NNO phase and the non-volatile phase transformation were also identified. We can see that after the phase transformation and removal of external elec-

tric field, it remains stable even after twenty days with invariable diffraction peak intensity and position (Figure S7, Supporting Information). Besides, for NNO films with different thicknesses, they display the same lattice expansion during the phase transformations, which further indicates that the giant lattice expansion takes place in the whole bulk film instead of the surface (Figure S8, Supporting Information). In situ XRD with heating was also performed to test the thermal stability of the H-NNO phase. The result shows that the H-NNO does not disappear until the temperature is increased to above ≈150 °C, and finally returns to the pristine NNO phase (Figure S9, Supporting Information). In addition, hydrogen-intercalation-induced lattice expansion was also carried out on the epitaxial thin films grown on $(LaAlO_3)_{0.3}–(SrAl_{0.5}Ta_{0.5}O_3)_{0.7}$ (001) (LSAT) and $SrTiO_3$ (001) (STO) substrates with the tensile strain of 1.6% and 2.6%, respectively (Figure 1f, Figures S10 and S11, Supporting Information). They show similar phase transformations, but with smaller lattice expansion of 11.4% and 10.1%, respectively. The decrease in the magnitude of lattice expansion upon hydrogenation observed for tensile strained films might be owing to their larger initial volume and different strain states. Through comparing with previous results of intercalation with H^+, O^{2-} and Li^+ ions, such a lattice expansion of H-NNO reaches a record value among oxide materials (Figure S12, Supporting Information).

**ADVANCED
SCIENCE NEWS**

www.advancedsciencenews.com

**ADVANCED
MATERIALS**

www.advmat.de
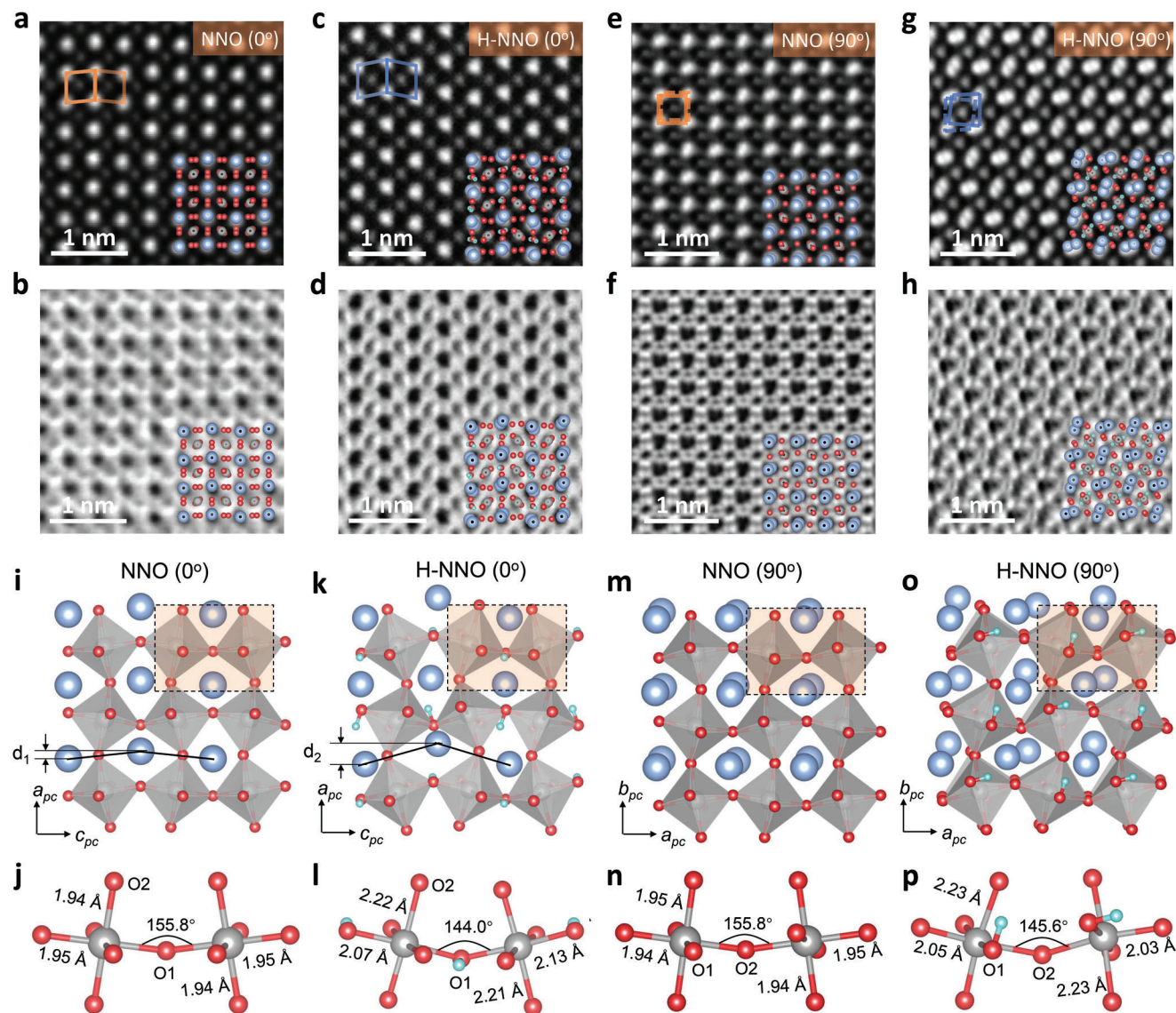
Figure 2. Real-space and atomic-scale demonstration of the lattice distortion and oxygen octahedra tilting/rotation upon hydrogen-ion intercalation. a–d) HAADF and ABF images of the NNO epitaxial thin film and the obtained H-NNO along the $[110]_o$ projection (0°), in which the local lattice distortion can be clearly identified. Insets show the calculated lattice structure with oxygen octahedral rotation and tilting which display the very consistent results to the measured STEM. e–h) HAADF and ABF images of the NNO and H-NNO along the $[001]_o$ projection (90°), where the Nd atom columns split, and the lattice symmetry changes from orthorhombic to monoclinic after hydrogen intercalation. i–p) Calculated atomic structure variation of NNO (i,j and m,n) and H-NNO (k,l and o,p) along the two projections ($[110]_o$ and $[001]_o$ or b_{pc} and c_{pc}) with the enhanced oxygen tiltings and rotations and decreased Ni–O–Ni bond angles. The blue, gray, red and cyan atoms represent the Nd, Ni, O and H atoms, respectively. The zigzag distortion of Nd atoms is marked by black lines, with the vertical distance of Nd atoms labeled by d_1 for NNO and d_2 for H-NNO, respectively. The Ni–O bond lengths (L) and Ni–O–Ni bond angles (θ) in two adjacent Ni–O octahedra are labeled in the lower panel. The oxygen atoms locating at the apical and equatorial position of octahedra along the $[001]_o$ projection are labeled as O1 and O2, respectively.

2.2. Real-Space and Atomic-Scale Observation of the Lattice Distortion and Oxygen Octahedra Tilting and Rotation in H-NNO

To provide the atomic scale lattice change by hydrogen-ion intercalation, structural investigations were performed by the state-of-the-art scanning transmission electron microscopy (STEM) (**Figures 2**a–h and Figures S13–S16, Supporting Information). In addition, to have a direct comparison between the real space STEM images, the calculated lattice structures with correspond-

ing oxygen polyhedral deformation are also shown in insets for reference. In the high-angle annular dark-field (HAADF) images, the atomic column intensities are approximately proportional to the square of the atomic number Z of each element. Thus, the atom columns comprising of Nd have a stronger intensity, while the Ni columns have a weaker intensity, and the O columns are barely visible. Complementary to HAADF, annular bright-field (ABF) imaging is relatively sensitive to light elements, thus oxygen atoms can be identified. To directly display the hydrogen

ADVANCED
SCIENCE NEWS
www.advancedsciencenews.com

ADVANCED
MATERIALS
www.advmat.de

intercalation effect on the NNO lattice, we show the STEM images of the pristine and hydrogenated lattice. In NNO with orthorhombic structure that can be related to pseudocubic unit cell through the following relationships of $[1-10]_o = a_{pc}$, $[110]_o = b_{pc}$, $[001]_o = c_{pc}$, there exists slight oxygen octahedral rotations and tiltings, as the $a^- a^- c^+$ tilt system in Glazer notation, corresponding to the rotation and tilting along the pseudocubic a_{pc}, b_{pc}, and c_{pc}-axes, respectively. The differing a and c specify unequal rotation angles and the superscript "+" or "−" indicates in-phase (in the same direction) or out-of-phase (in the opposite direction) rotation of the two adjacent octahedra along the corresponding crystal axis. Corresponding to the $a^- a^- c^+$ oxygen octahedral tilting, the $[001]_o$ axis of the NNO orthorhombic unit cell is the special in-phase rotation axis. Due to lower lattice mismatch, the preferred growth orientation is expected to be $[001]_o$ in-plane for NNO grown on LAO (001) substrate. In our samples, two distinct orthorhombic domains labeled as 0° ($[110]_o$) and 90° ($[001]_o$) could be identified with 90° rotation, which correspond to the in-phase $[001]_o$ axis perpendicular and parallel to the electron beam direction of the STEM (Figure S14, Supporting Information).[26] Based on these, we investigate the hydrogen ion intercalation induced lattice distortion for the two cases, respectively.

Firstly, for the $[110]_o$ projection (0° domain) (Figures 2a–d), the averaged lattice spacing (3.82 Å) of pristine NNO agrees well with the XRD result (Figure 2a). Due to the oxygen octahedral tilting, the Nd atoms at the A site are staggered vertically (marked in Figures 2a,b). With hydrogen-ion intercalation, the Ni–O octahedra tilt dramatically. Compared with the pristine pseudocubic NNO, intensive zigzag Nd atom chains due to increased octahedral tilting in the H-NNO phase are formed (Figure 2c,d). Moreover, the intensity profile of H-NNO suggests a much larger lattice constant compared with that of the pristine NNO, with an averaged spacing of 4.3 Å, implying a lattice expansion up to ≈13% that is consistent with the macroscopic XRD measurement (Figure 1c and Figure S16, Supporting Information). Additionally, the electron energy loss spectra (EELS) of O K and Ni $L_{2,3}$ edges were also performed and the change of electron states of Ni and O further confirms the ionic-intercalation-induced phase transformation (Note 3 and Figure S17, Supporting Information). While for the $[001]_o$ projection (90° domain) (Figure 2e–h), the notable characteristic is two overlap types of staggered Nd atoms. For NNO, it shows different oxygen rotation pattern that the zigzag oxygen atom chain can be clearly identified, and displays slightly separated Nd atom columns (Figure 2e,f). With hydrogen-ion intercalation, we found that the quasi-square structure distorts obliquely changing from orthorhombic to monoclinic (Figure 2g,h, Figures S15 and S16, Supporting Information). Moreover, with more significant oxygen octahedra tilting, the two different overlap types of Nd atoms become more noticeable because the separation among the staggered Nd atoms in the same projected atom column also become larger. Based on above results, we know that along $[110]_o$ and $[001]_o$ projections, with enhanced Ni–O octahedra rotation and dramatically deformed Nd atomic column induced by hydrogen intercalation, the Ni–O bonds length increases and the lattice expands, which would lead to distinct electronic structures through changing the orbital overlap.

To further confirm the hydrogen-ion-induced phase transformation and lattice deformation in H-NNO, we carried out density functional theory (DFT) calculations. The lattice structure of

NNO and hydrogenated H-NNO with two projections are shown respectively (Figure 2i–p and Figures S18–S20, Supporting Information). We have investigated the atomic configurations upon hydrogenation and found that the most stable configuration has hydrogens connected to apical oxygens of the oxygen octahedra along the in-phase $[001]_o$ axis. The hydrogen-ion intercalation to NNO induces remarkable volume expansion and extreme structural distortion. However, the hydrogen intercalation does not change the oxygen octahedral rotation pattern, but only increases rotation angles (Figure 2k,o). Upon hydrogenation, the most notable change of lattice structure is the increased zigzag deformation of Nd atoms for the $[110]_o$ projection (0° domain), with the vertical distance of two adjacent Nd atoms (labeled as d_1 and d_2 in Figure 2i,k, respectively) increasing from ≈0.39 Å to ≈1.12 Å. Meanwhile, the tiltings of NiO_6 octahedra are increased due to the cooperative interaction of the left and right corner hydrogen atoms at the oxygen octahedra (Figure S19, Supporting Information). As shown in Figure 2j,l, the Ni–O–Ni bond angle (θ) is reduced by ≈11.8° from 155.8° to 144.0°, the average Ni–O bond length (L) is increased by ≈0.18 Å and the variation between Ni–O bond lengths in one octahedra (ΔL) is also obviously increased. The intensified lattice distortion of NiO_6 octahedra changes the overlapping between Ni 3d and O 2p orbitals, which would strongly affect the electronic structure of H-NNO.[27] While for the $[001]_o$ projection (90° domain), the tiltings of oxygen octahedra are enhanced due to the intercalated hydrogen ions that bond to the apical oxygen atoms, which further leads to the increased splitting of Nd atoms in the same atom columns (Figure 2m,o). Accordingly, in this lattice direction, the Ni–O–Ni bond angle also reduces largely by ≈10.2° (Figure 2n,p).

2.3. Electronic-Antidoping-Induced Metal–Insulator Transition with Hydrogen-Ion Intercalation

Based on the real space and atomic scale lattice variation, we next focus on the hydrogen-intercalation-induced electronic structure change and its influence on the physical properties. As shown in **Figure 3**a, the as-grown high-quality NNO show sharp temperature-driven first order metal–insulator transition,[11,28] and upon hydrogen-ion intercalation the metal–insulator transition with seven orders of magnitude in electrical resistivity change can be observed. Figure 3b shows the optical transmittance before and after hydrogen-ion intercalation, from which we can see that the transmittance is nearly linearly proportional to the thin-film thickness for the pristine samples, while after gating, the transmittance is almost insensitive to the thickness. The results indicate that with hydrogen intercalation the energy bandgap is open and its value is beyond the measured optical energy range.

To probe the doping-induced band filling through hydrogen-ion intercalation, we carried out the soft X-ray absorption spectroscopy (XAS) measurements near the Ni L-edge and O K-edge of NNO and H-NNO. The Ni L-edge XAS (2p to 3d transition) implies the transition metal 3d state in the compound and the O K-edge XAS corresponds to transitions from 1s to unoccupied O 2p states above Fermi level. Specifically, due to the metal-oxygen hybridization or charge transfer from O to transitional metal Ni, the O K-edge also reflects the 3d characteristics of Ni element.[19,29]

**ADVANCED
SCIENCE NEWS**

www.advancedsciencenews.com

**ADVANCED
MATERIALS**

www.advmat.de
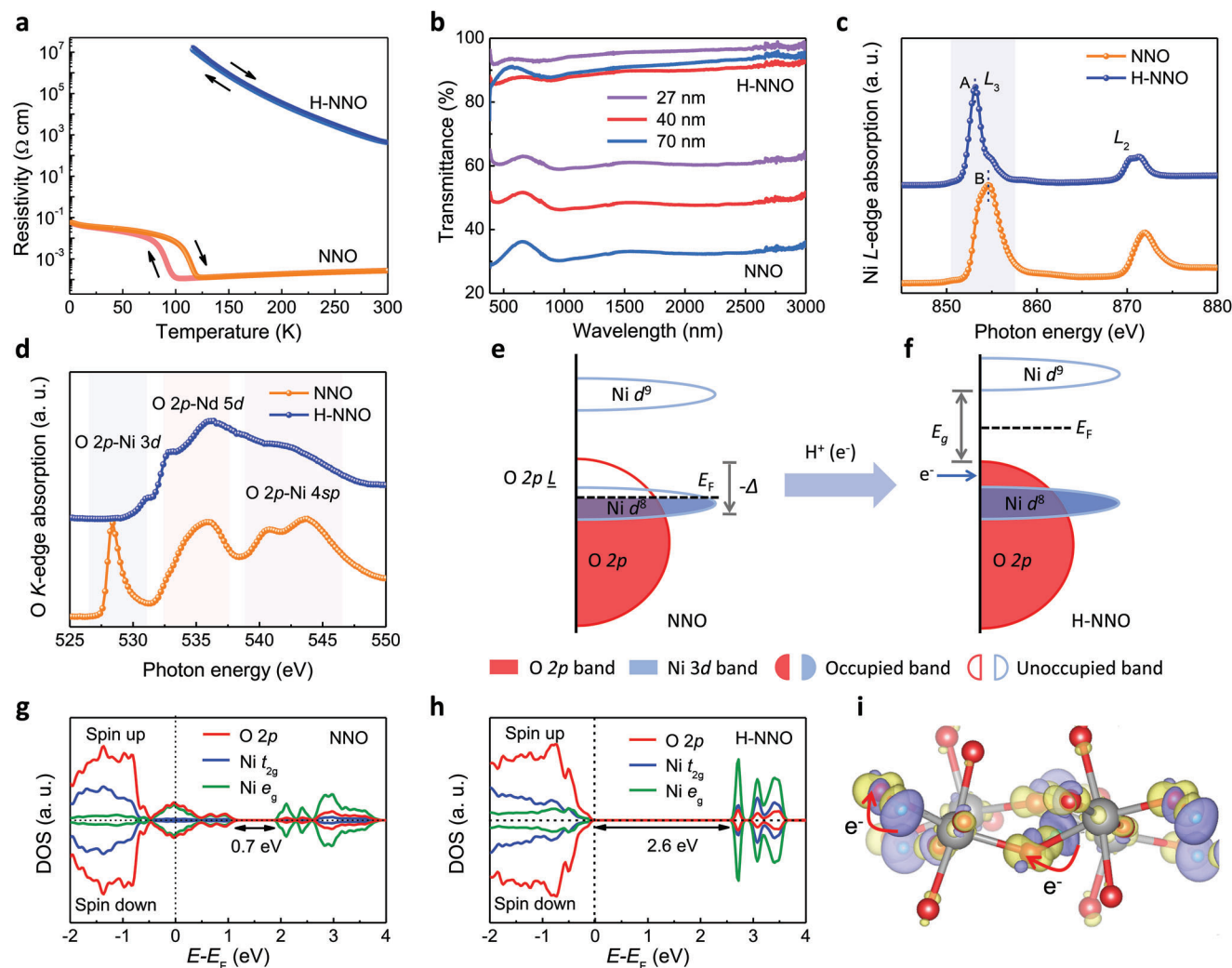
Figure 3. Electronic-antidoping-induced metal–insulator transition. a) Temperature-dependent electrical resistivity and metal–insulator transition with hydrogen-ion intercalation. b) Optical transmittance of the pristine NNO and hydrogenated H-NNO. c,d) Soft X-ray absorption spectra of the Ni L-edge and O K-edge of the pristine and hydrogen-intercalated H-NNO phase. We can see that with hydrogen-ion intercalation, the peak of feature A (3d^8-like configuration) in the Ni L-edge remains well while the feature B (ligand hole $\underline{L}$) disappears, meanwhile the pre-peak of O K-edge representing the orbital hybridization of O 2p–Ni 3d also disappears. e,f) Energy band structure variation before and after hydrogen intercalation, in which the doped electron occupies the empty Ni–O hybrid orbital, where Δ represents the charge-transfer energy from O 2p to Ni 3d. g,h) Spin-polarized projected density of states (PDOS) for NNO and H-NNO phases, respectively. Upon hydrogenation, metallic NNO is transformed to the insulating H-NNO with bandgap of 2.6 eV. The transition energy from Ni 3d^8 configuration to Ni 3d^9 configuration is labeled by black arrows. i) Electron-doping effect induced by hydrogenation. The valence electrons of H atoms are transferred to the nearest O atom (labeled by red arrow), with the yellow (blue) areas representing the increased (decreased) charge density with isosurface 7×10^{-2} e Å^{-3}.

It is revealed that the Ni L_3 region of the XAS is characterized by two features (A and B), with feature A representing the d^8-like configuration of Ni in NNO and feature B mainly indicating the ligand hole states around the Fermi level (Figure 3c).[30,31] As for the O K-edge, it shows three different peaks, corresponding to Ni 3d, Nd 5d and Ni 4sp orbitals hybridizing with O 2p orbital, respectively (Figure 3d).

For H-NNO phase, the XAS spectra show that both the feature B of Ni L_3-edge and pre-edge of O K-edge below 530 eV (empty state above the Fermi level of the O 2p orbital) disappear completely after hydrogenation due to electron doping, which is also consistent with results of the EELS spectra that focus on local structure in the STEM measurement (Figure S17, Supporting In-

formation). Besides, because the enhanced octahedral tilting or rotation suppresses the Ni–O orbital overlap, the Ni 4sp–O 2p hybridization part in O K-edge is also weakened. Figure 3e,f show the schematic diagrams of the energy band structure before and after hydrogen intercalation. Due to the negative charge-transfer energy Δ in the Zaanen–Sawatzky–Allen scheme, the Fermi level goes cross the Ni 3d and O 2p hybrid orbitals.[32,33] The lowest unoccupied band shows mainly ligand-hole character and NNO behaves like a metal. After gating, the doped electrons fill the empty states of the hybrid orbitals along with hydrogen-ion intercalation, and thus the Fermi level is shifted to the bandgap between O 2p and upper Ni 3d Hubbard band. In such ways, H-NNO becomes a positive charge-transfer insulator (no ligand holes) and

ADVANCED
SCIENCE NEWS
www.advancedsciencenews.com

**ADVANCED
MATERIALS**
www.advmat.de

the metal–insulator transition could be explained by the electronic antidoping mechanism. Conventionally, electron doping shifts the Fermi level to the conduction band and increases the conductivity of semiconductors. The antidoping concept is proposed that doped electrons fill the lowest unoccupied band and lead to a decrease in electric conductivity.[34] In the present work, we find that it is not a simple process that intercalated hydrogen ions change the valance state of Ni from +3 to +2, but involves electron filling of the negative charge transfer dominated O ligand-hole states. In addition, the strain dependent H-NNO and nickelate with Sm as A site ($SmNiO_3$) also show the same results, which further indicate the antidoping mechanism for the metal–insulator transition of hydrogenated perovskite nickelates (Figures S21 and S22, Supporting Information). Moreover, comparing the Ni L-edge XAS of H-NNO and NiO, we notice that they show the same features which imply one electron doping per pseudocubic lattice in H-NNO (Figure S23, Supporting Information). This result further indicates the nearly stoichiometric ratio of hydrogenated NNO (H: NNO ≈ 1:1).

Furthermore, the mechanism of metal–insulator transition upon hydrogenation is also analyzed by means of the projected density-of-states (PDOS) based on first-principle calculations (Figure 3g–i). The previous work [35,36] has confirmed the validity of Ni^{2+} $3d^8\underline{L}$ configuration, where $\underline{L}$ represents the oxygen ligand-hole, instead of the formal Ni^{3+} $3d^7$ configuration suggested by the ionic model of NNO. We find that both the occupied and unoccupied electronic states around the Fermi level of NNO are composed of the Ni e_g and O 2p states, where the O 2p states have more projected weights, suggesting the rationality of $3d^8\underline{L}$ configuration and the strong Ni–O hybridization. Based on this recognition, the doped electrons during hydrogen intercalation mainly fill the oxygen 2p holes instead of occupying the Ni e_g orbital, which is also confirmed by the different charge density distribution ($\Delta\rho = \rho_{HNNO} - \rho_{NNO} - \rho_{H-atom}$), as shown in Figure 3i. For doping concentration with 1H per f.u., the Ni–O hybridized states above the Fermi level are fully filled, resulting in the reconstruction of the valance and conduction bands. Meanwhile, the Coulomb repulsion energy for transition from Ni $3d^8$ to $3d^9$ configuration (labeled by black arrows in Figure 3g,h), is enlarged from ≈0.7 eV for the NNO to ≈2.6 eV for the H-NNO. The doping concentration dependence of metal–insulator transition (see Figure S20, Supporting Information) shows that the filling degree of O 2p empty states and the Coulomb repulsion energy increases with the increased doping concentration of hydrogens. These two effects, i.e., filling of oxygen holes and enhancement of Coulomb repulsion upon hydrogenation together induce the formation of insulating H-NNO with the large bandgap.

Since both the charge doping and lattice distortions would have influence on the electronic structure of H-NNO, to identify the relative importance of these two effects, we simulated the cases of pure electron doped NNO (e-NNO) with pristine lattice structure and the lattice distortive NNO without hydrogenation, and the corresponding PDOS are shown in Figures S24 and S25 (Supporting Information), respectively. The e-NNO is also an insulating phase with bandgap of ≈2.5 eV comparable to that of the H-NNO, and the lattice distortion with the enhanced octahedral tilting or rotation only changes the orbital weight of electronic states near the Fermi level (Figure 3h and Figure S25, Supporting Information). The distinct variation of electronic structure

induced by the individual electron doping or lattice deformation indicates that the former plays an essential role in the metal–insulator transition upon hydrogenation.

2.4. Demonstration of the Strong Ion–Electron–Lattice Coupling by Hydrogen Ion Intercalation Controlled Selective Micropatterns

Based on above results, to further demonstrate the strong coupling among the hydrogen-ion intercalation, lattice expansion and metal–insulator transition, we fabricate the micropattern by employing the synergistic effect of ion diffusion via the liquid-solid interface and electron compensation through the electrode–film interface during gating.[19] We prepared the NNO film with pre-patterns through photolithography, and then the ionic liquid gating was carried out before removal of the residual photoresist (Figure S26, Supporting Information). The conducting AFM mappings of the pristine region (NNO film) and gated region (H-NNO film) were measured (**Figure 4**a,b). Figure 4a,c shows the giant lattice expansion induced by hydrogen intercalation. From the result, we know that the expansion height of the gating region is ≈3.3 nm, then based on the thin-film thickness of 24 nm, the expansion of the micropattern by ≈13% is nicely consistent with the macroscopic XRD results. Figure 4b,d shows the corresponding electric conductance change of the same pattern. It is obvious that the huge resistance difference (or electric potential difference) was obtained between pristine and hydrogenated region. The I–V curves of the pristine and gated region shown in Figure 4e also indicate the modulation of electrical property. Then, by taking advantage of the strong ion–electron–lattice coupling, we fabricate a micropattern with distinct surface profile and electric conductivity (Figure 4f). These results indicate that the ionic intercalation can be artificially controlled at micrometer or even nanometer scale to fabricate micro devices with controlled lattice structure and electric conductivity.

3. Conclusion

By using ionic liquid gating, we achieve electric-field-controlled hydrogenated NNO and identify that this new robust phase is stoichiometric H-NNO due to its fixed crystal structure and electronic states. We demonstrate the reversible phase transformation between NNO and HNNO, in which the maximum lattice expansion can reach up to 13.2% for the epitaxial film on LAO substrate. With atomic-scale lattice analysis, the hydrogenated NNO crystal structure was clearly identified. The results show that the hydrogenated phase accommodates the increased bonds through dramatic lattice deformation and enhanced oxygen octahedra tilting/rotation. Moreover, combining the soft X-ray absorption spectra and theoretical calculations, the underlying metal–insulator transition is identified to be the electron antidoping mechanism that the doped electrons mainly fill the oxygen 2p holes instead of changing Ni oxidation state from Ni^{3+} to Ni^{2+}, contrary to the previously proposed redox reaction mechanism. Furthermore, from the hydrogen-ion intercalation induced lattice expansion and metal–insulator transition, we realize the selective micropattern fabrication by employing the synergistic effect during ionic liquid gating. We envision that the

**ADVANCED
SCIENCE NEWS**

www.advancedsciencenews.com

**ADVANCED
MATERIALS**

www.advmat.de
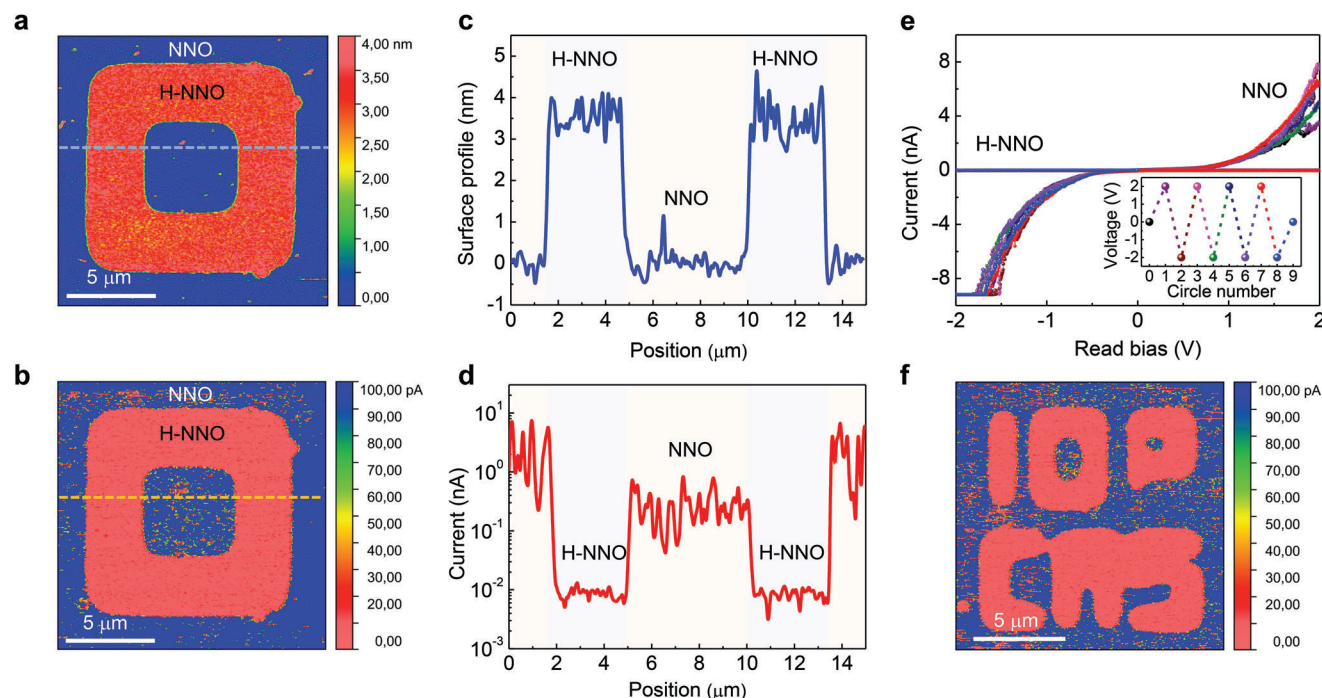
Figure 4. Strong ion–electron–lattice coupling demonstration by hydrogen ion intercalation controlled selective micropatterns. a) Microscopic profile pattern of the origin NNO and H-NNO, from which we can clearly identify the nanolevel lattice expansion. b) Electric conductivity variation with hydrogen intercalation. c) Profile of the lattice expansion in (a). The expansion height is ≈3.3 nm and the thin-film thickness is 24 nm. The 13% lattice expansion is consistent with the XRD measurement. d) Conductive profile corresponding to the surface profile in (c), in which the NNO shows low resistance and H-NNO displays high resistance. e) I–V curves of the pristine and gated areas in (b), in which obviously different electric resistivity can be identified for the distinct phases. f) Electric-field-controlled hydrogen-intercalation-induced micropattern "IOP CAS" with the different electric conductance and surface profile.

electric-field-controlled ionic intercalation based on strong ion–electron–lattice coupling offers us a powerful pathway to design new materials and devices with desirable functionalities.

4. Experimental Section

Thin-Film Growth and Measurements: Thin films were grown by a self-designed pulsed laser deposition system, at a growth temperature of 600 °C and an oxygen pressure of 10 Pa. The energy density of the krypton fluoride excimer laser ($\lambda = 248$ nm) was fixed at 2.0 J cm^{-2} at the neodymium nickelate ceramic target, with a repetition rate of 2 Hz. After growth, the samples were cooled to room temperature at a cooling rate of 10 °C per min in 10 Pa oxygen pressure. The thickness of each sample was controlled by the growth time, and confirmed with X-ray reflectometry measurements.

XRD Characterization and In Situ XRD Measurements: The crystalline structure of the films (see Figure 1c) was characterized by using a high-resolution four-circle X-ray diffractometer (Smartlab, Rigaku), which displays the phase transformation and confirms that the obtained thin films were coherently strained on the substrate with high crystalline quality. For in situ XRD measurement (Figure 1d), the edges of the thin films were painted with silver conductive adhesive before ionic liquid gating which forms the bottom electrode. Subsequently, conductive platinum wires were fixed on the conductive electrode, and a platinum plate was used as the gate electrode. During the in situ XRD measurements, the sample was first aligned with the substrate (002) peak without the ionic liquid, then a small drop of ionic liquid (*N,N*-diethyl-*N*-(2-methoxyethyl)-*N*-methylammonium bis(trifluoromethylsulfonyl)imide-DEME-TFSI) was added to cover both the film surface and the platinum plate. The gating

voltage was set to 0 V at the start, and ramped to the desired voltage, and maintained until the phase transformations were completed, while XRD spectra were collected continuously, with a scanning rate 6° min^{-1} and a diffraction pattern per 2 min.

Pt Catalytic Hydrogenation: A 20 nm Pt film was deposited on perovskite nickelate thin film by magnetron sputtering. The samples were loaded in a home-made annealing chamber and kept 1 h in forming gas atmosphere (5% H$_2$ in Ar). After hydrogenation, the Pt layer on the sample surface was wiped off, and following characterizations were carried out.

STEM Characterization: STEM sample was prepared by using Focused Ion Beam (FIB) milling. Cross-sectional lamella was thinned down to 100 nm-thick at an accelerating voltage of 30 kV with a decreasing current from the maximum 2.5 nA, followed by fine polish at an accelerating voltage of 2 kV with a small current of 40 pA. The atomic structures of the NNO and H-NNO films were characterized using an ARM-200CF (JEOL, Tokyo, Japan) transmission electron microscope operated at 200 kV and equipped with double spherical aberration (Cs) correctors. HAADF and ABF images were acquired at acceptance angles of 90–370 mrad and 12–24 mrad, respectively.

Soft X-ray Absorption (sXAS) Measurements: The soft XAS measurements of Ni *L*-edge and O *K*-edge in total electron yield mode were carried out (Beamline 4B9B of Beijing Synchrotron Radiation Facility) to identify the electric-field-controlled hydrogen-intercalation-induced phase transformation. The size of synchrotron-radiation X-ray spot on samples is 2 mm × 0.5 mm. The XAS spectra have been normalized to the photon flux measured by the photocurrent of a clean gold mesh. Because Ni *L*-edge XAS measurement corresponds directly to 2p to 3d transition, the strong variation in line shape among the two phases provides unambiguous experimental evidence for the change of the unoccupied state. Moreover, due to the hybridization between the nickel and oxygen atoms, the O

K-edge also reflect the electron occupation condition of the O 2p and Ni 3d orbitals during the phase transformation.

Secondary-Ion Mass Spectroscopy Measurements: To obtain information about the hydrogen concentration of H-NNO, we carried out secondary-ion mass spectrometry (SIMS) measurement in the negative ion mode (IONTOF GmbH) (see Figure 1e), whose mass resolution is ≈4000 atomic mass units (full-width at half-maximum). During the measurement, to avoid disturbance from the crater edge, the sputtering area was 350×350 μm^2, and the SIMS data were collected only in an area of 100×100 μm^2 within that region with Bi-ion analysis beam.

Electronic Transportation and Optical Transmittance Measurements: We used a physical property measurement system (PPMS; Quantum Design) to measure the temperature-dependent electrical resistivity of pristine and gated NNO thin-film samples with a four-probe method (to eliminate contact resistance). For the optical transmittance measurement, we used thin films with different thickness grown on double-sided polished LAO (001) substrate for the optical measurements. For reference, we used a bare LAO substrate that had been processed through the same thermal cycles as the sample growth. Optical transmittance spectra were taken in air at room temperature with spectrophotometers (Cary 5000 UV–Vis–NIR, Agilent), covering the visible and infrared range with wavelengths between 380 nm and 3000 nm (Figure 3b).

Theoretical Calculation: First-principles calculations were performed within the DFT+U approximations with the Vienna ab initio simulation package (VASP).[37] The Perdew–Burke–Ernzerhof (PBE) exchange-correlation functional [38] and the projector-augmented wave (PAW) pseudopotentials with Nd_3 (valence $5s^2 5p^2 6s^2 4f^1$), Ni_pv (valence $3p^6 4s^2 3d^8$), O (valence $2s^2 2p^4$) and H (valence $1s^1$) were adopted. The rotationally invariant LDA+U was chosen to describe the localized d electrons of the Ni atoms,[39] with the effective onsite Coulomb and exchange parameters $U = 4.6$ eV and $J = 0.6$ eV. We start from the orthorhombic (Pbnm) phase of NdNiO$_3$ and based on it make the $\sqrt{2} \times \sqrt{2} \times 1$ supercell with cubic symmetry containing 40 atoms. The Brillouin zone is sampled by 5×5×5 Monkhorst–Pack k-mesh, and the plane-wave energy cutoff of 500 eV was applied. Geometry optimization was carried out until the residual force on each atom was less than 0.02 eV Å^{-1}. To determine the structure of H-NNO, we begin with the atomic configuration of H$_{0.25}$NNO. In structural relaxation, to mimic the constraint effect of substrate, we fix the lattice parameters along the [001]$_o$ and [110]$_o$-axes and search the optimized lattice parameter along the *c*-axis with the lowest total energy, and then relax the ionic positions with fixed cell parameter. These calculations were carried out in the same experimentally observed orientation relationship. The structure with the lowest total energy was chosen (Figure 2i,m), and based on it we can construct H$_{0.5-1}$NNO via finding the symmetry-equivalent site of relaxed hydrogen position.

Scanning Probe Microscopy Characterization: The scanning probe microscopy (SPM) measurements were carried out (Cypher ES, Oxford Instruments), which was armed with Pt-coated conductive cantilevers (HQ: NSC18/Pt, MikroMasch) with a spring constant of ≈2.8 N m^{-1} and a free resonance frequency of ≈75 kHz. Thin films for SPM imaging were glued on a conductive sample plate with silver epoxy, which was grounded as the bottom electrode during measurements. The current mapping and *I–V* curves were measured by an integrated commercial conductive atomic force microscopy (C-AFM) mode of the SPM system. The current mapping was carried out with a fixed tip voltage of 0.1 V.

Supporting Information

Supporting Information is available from the Wiley Online Library or from the author.

Acknowledgements

Conflict of Interest

The authors declare no conflict of interest.

Author Contributions

L.G. and H.W. contributed equally to this work. N.L. and L.G. conceived the project and designed the experiments. L.G. grew the sample and performed the X-ray diffraction, electronic transport, optical transmittance, secondary-ion mass spectroscopy and soft X-ray absorption measurements with help from X.L., M.Z., Y.W., C.L., J.L. and A.J. Q.Z., F.M. and T.L. performed the scanning transmission electron microscopy measurements under the supervision of L.Gu. H.W. performed the first-principle calculations under the supervision of S.M. H.P. performed the conducting atomic force microscopy under the supervision of P.Y. Z.C. discussed the results. L.G, and N.L. wrote the manuscript with input from all authors. All authors have discussed the results and commented on the manuscript.

Data Availability Statement

The data that support the findings of this study are available from the corresponding author upon reasonable request.

Keywords

[1] H. Y. Hwang, Y. Iwasa, M. Kawasaki, B. Keimer, N. Nagaosa, Y. Tokura, *Nat. Mater.* **2012**, *11*, 103.

[2] S. Z. Bisri, S. Shimizu, M. Nakano, Y. Iwasa, *Adv. Mater.* **2017**, *29*, 1607054.

[3] A. J. Tan, M. Huang, C. O. Avci, F. Büttner, M. Mann, W. Hu, C. Mazzoli, S. Wilkins, H. L. Tuller, G. S. D. Beach, *Nat. Mater.* **2019**, *18*, 35.

[4] N. Lu, P. Zhang, Q. Zhang, R. Qiao, Q. He, H.-B. Li, Y. Wang, J. Guo, D. Zhang, Z. Duan, Z. Li, M. Wang, S. Yang, M. Yan, E. Arenholz, S. Zhou, W. Yang, L. Gu, C.-W. Nan, J. Wu, Y. Tokura, P. Yu, *Nature* **2017**, *546*, 124.

[5] Q. Lu, S. Huberman, H. Zhang, Q. Song, J. Wang, G. Vardar, A. Hunt, I. Waluyo, G. Chen, B. Yildiz, *Nat. Mater.* **2020**, *19*, 655.

[6] L. Li, M. Wang, Y. Zhang, Y. Zhang, F. Zhang, Y. Wu, Y. Wang, Y. Lyu, N. Lu, G. Wang, H. Peng, S. Shen, Y. Du, Z. Zhu, C.-W. Nan, P. Yu, *Nat. Mater.* **2022**, *21*, 1246.

[7] N. P. Lu, Z. Zhang, Y. J. Wang, H. B. Li, S. Qiao, B. Zhao, Q. He, S. C. Lu, C. Li, Y. S. Wu, M. T. Zhu, X. Y. Lyu, X. K. Chen, Z. L. Li, M. Wang, J. Z. Zhang, S. C. Tsang, J. W. Guo, S. Z. Yang, J. B. Zhang, K. Deng, D. Zhang, J. Ma, J. Ren, Y. Wu, J. Y. Zhu, S. Y. Zhou, Y. Tokura, C. W. Nan, J. Wu, et al., *Nat. Energy* **2022**, *7*, 1208.

[8] M. Imada, A. Fujimori, Y. Tokura, *Rev. Mod. Phys.* **1998**, *70*, 1039.

[9] D. Khomskii, *Transition Metal Compounds*, Cambridge University Press, Cambridge, UK **2014**.

[10] C. G. Granqvist, *Thin Solid Films* **2014**, *564*, 1.

[11] S. Catalano, M. Gibert, J. Fowlie, J. Íñiguez, J.-M. Triscone, J. Kreisel, *Rep. Prog. Phys.* **2018**, *81*, 046501.

[12] I. I. Mazin, D. I. Khomskii, R. Lengsdorf, J. A. Alonso, W. G. Marshall, R. M. Ibberson, A. Podlesnyak, M. J. Martínez-Lope, M. M. Abd-Elmeguid, *Phys. Rev. Lett.* **2007**, *98*, 176406.

[13] S. Middey, J. Chakhalian, P. Mahadevan, J. W. Freeland, A. J. Millis, D. D. Sarma, *Annu. Rev. Mater. Res.* **2016**, *46*, 305.

[14] R. Scherwitzl, P. Zubko, I. G. Lezama, S. Ono, A. F. Morpurgo, G. Catalan, J.-M. Triscone, *Adv. Mater.* **2010**, *22*, 5517.

[15] Y. Zhou, X. Guan, H. Zhou, K. Ramadoss, S. Adam, H. Liu, S. Lee, J. Shi, M. Tsuchiya, D. D. Fong, S. Ramanathan, *Nature* **2016**, *534*, 231.

[16] Z. Zhang, D. Schwanz, B. Narayanan, M. Kotiuga, J. A. Dura, M. Cherukara, H. Zhou, J. W. Freeland, J. Li, R. Sutarto, F. He, C. Wu, J. Zhu, Y. Sun, K. Ramadoss, S. S. Nonnenmann, N. Yu, R. Comin, K. M. Rabe, S. K. R. S. Sankaranarayanan, S. Ramanathan, *Nature* **2018**, *553*, 68.

[17] H.-T. Zhang, T. J. Park, A. N. M. Nafiul Islam, D. S. J. Tran, S. Manna, Q. Wang, S. Mondal, H. Yu, S. Banik, S. Cheng, H. Zhou, S. Gamage, S. Mahapatra, Y. Zhu, Y. Abate, N. Jiang, S. K. R. S. Sankaranarayanan, A. Sengupta, C. Teuscher, S. Ramanathan, *Science* **2022**, *375*, 533.

[18] J. Chen, W. Mao, B. Ge, J. Wang, X. Ke, V. Wang, Y. Wang, M. Döbeli, W. Geng, H. Matsuzaki, J. Shi, Y. Jiang, *Nat. Commun.* **2019**, *10*, 694.

[19] L. Gao, X. K. Chen, X. Y. Lyu, G. P. Ji, Z. F. Chen, M. T. Zhu, X. Cao, C. R. Li, A. L. Ji, Z. X. Cao, N. P. Lu, *J. Phys.: Condens. Matter* **2021**, *33*, 104004.

[20] C. Leighton, *Nat. Mater.* **2019**, *18*, 13.

[21] Y. Zhao, X. Li, B. Yan, D. Xiong, D. Li, S. Lawes, X. Sun, *Adv. Energy Mater.* **2016**, *6*, 1502175.

[22] A. S. Andersson, B. Kalska, L. Häggström, J. O. Thomas, *Solid State Ionics* **2000**, *130*, 41.

[23] S. R. Bishop, D. Marrocchelli, C. Chatzichristodoulou, N. H. Perry, M. B. Mogensen, H. L. Tuller, E. D. Wachsman, *Annu. Rev. Mater. Res.* **2014**, *44*, 205.

[24] H. Ren, A. I. Osaka, A. N. Hattori, B. Yu, M. Nagai, M. Ashida, B. Li, C. Zou, H. Tanaka, *ACS Appl. Electron. Mater.* **2022**, *4*, 3495.

[25] J. Shi, Y. Zhou, S. Ramanathan, *Nat. Commun.* **2014**, *5*, 4860.

[26] A. Vailionis, H. Boschker, W. Siemons, E. P. Houwman, D. H. A. Blank, G. Rijnders, G. Koster, *Phys. Rev. B* **2011**, *83*, 064101.

[27] B. Chen, N. Gauquelin, R. J. Green, J. H. Lee, C. Piamonteze, M. Spreitzer, D. Jannis, J. Verbeeck, M. Bibes, M. Huijben, G. Rijnders, G. Koster, *Nano Lett.* **2021**, *21*, 1295.

[28] J. Chen, H. Hu, J. Wang, T. Yajima, B. Ge, X. Ke, H. Dong, Y. Jiang, N. Chen, *Mater. Horiz.* **2019**, *6*, 788.

[29] M. Hepting, D. Li, C. J. Jia, H. Lu, E. Paris, Y. Tseng, X. Feng, M. Osada, E. Been, Y. Hikita, Y.-D. Chuang, Z. Hussain, K. J. Zhou, A. Nag, M. Garcia-Fernandez, M. Rossi, H. Y. Huang, D. J. Huang, Z. X. Shen, T. Schmitt, H. Y. Hwang, B. Moritz, J. Zaanen, T. P. Devereaux, W. S. Lee, *Nat. Mater.* **2020**, *19*, 381.

[30] J. C. Fuggle, J. E. Inglesfield, Ed., *Unoccupied Electronic States*, Springer, Berlin/Heidelberg, Germany, **1992**.

[31] V. Bisogni, S. Catalano, R. J. Green, M. Gibert, R. Scherwitzl, Y. Huang, V. N. Strocov, P. Zubko, S. Balandeh, J.-M. Triscone, G. Sawatzky, T. Schmitt, *Nat. Commun.* **2016**, *7*, 13017.

[32] J. Zaanen, G. A. Sawatzky, J. W. Allen, *Phys. Rev. Lett.* **1985**, *55*, 418.

[33] T. Mizokawa, A. Fujimori, T. Arima, Y. Tokura, N. Mōri, J. Akimitsu, *Phys. Rev. B* **1995**, *52*, 13865.

[34] Q. Liu, G. M. Dalpian, A. Zunger, *Phys. Rev. Lett.* **2019**, *122*, 106403.

[35] M. Kotiuga, K. M. Rabe, *Phys. Rev. Mater.* **2019**, *3*, 115002.

[36] L. Iglesias, M. Bibes, J. Varignon, *Phys. Rev. B* **2021**, *104*, 035123.

[37] G. Kresse, J. Furthmüller, *Phys. Rev. B* **1996**, *54*, 11169.

[38] J. P. Perdew, K. Burke, M. Ernzerhof, *Phys. Rev. Lett.* **1996**, *77*, 3865.

[39] A. I. Liechtenstein, V. I. Anisimov, J. Zaanen, *Phys. Rev. B* **1995**, *52*, R5467.